The International Journal of Advanced Manufacturing Technology (2019) 102:1885–1900
https://doi.org/10.1007/s00170-018-03217-5

ORIGINAL ARTICLE

Geometrical simulation and analysis of ball-end milling surface topography

Li Shujuan[1] · Yongheng Dong[1] · Yan Li[1] · Pengyang Li[1] · Zhenchao Yang[1] · Robert G. Landers[2]

Received: 28 July 2018 / Accepted: 13 December 2018 / Published online: 15 January 2019

Abstract

Ball-end milling cutter has a strong adaptability and widely used in machining complex surface of parts. However, the geometry of ball-end milling cutter tooth is complex, and contact points between cutter tooth and part are varying constantly during milling process, which lead that it is difficult to study the surface topography by the traditional experimental method. Based on the time-step method, this paper proposes an improved Z-MAP algorithm to simulate the part surface topography after ball-end milling. On the basis of the cutter tooth movement equation established by homogeneous matrix transformation, the improved Z-MAP algorithm combines servo rectangular encirclement and the angle summation method to quickly obtain the instantaneous swept points that belong to the part, and introduce Newton iterative method to calculate the height of swept points. Comparing to traditional Z-MAP algorithm which discrete segments of cutter tooth can only sweep one discrete point of part during a unit time step, the proposed algorithm need not to disperse cutter tooth, accomplishes higher precision and efficiency. The influence of processing parameters, such as step over, feed per tooth, cutter posture, and cutter tooth initial phase angle difference, upon the surface topography and roughness are analyzed. The experiments are conducted to validate the availability of the proposed algorithm, and the results show that surface topographies simulated by the improved Z-MAP algorithm have a higher consistency with the experiments and costs less time than by the traditional Z-MAP algorithm under the same simulation conditions. Therefore, the proposed algorithm is effective for simulating the machined surface quality in practical production and rational selection of machining parameters.

Keywords Ball-end milling · Surface topography · Improved Z-MAP algorithm · Simulation analysis

✉ Li Shujuan
shujuanli@xaut.edu.cn

Yongheng Dong
DongYongheng@xaut.edu.cn

Yan Li
jyxy-ly@xaut.edu.cn

Pengyang Li
151812915@qq.com

Zhenchao Yang
79779304@qq.com; 405088489@qq.com

Robert G. Landers
landersr@mst.edu

[1] School of Mechanical and Instrument Engineering, Xi'an University of Technology, 5 South Jinhua Road, Xi'an 710048, Shaanxi, China

[2] Department of Mechanical and Aerospace Engineering, Missouri University of Science and Technology, Rolla, MO 65409–0050, USA

1 Introduction

With the development of high-precision manufacturing, part surface topography (i.e., the micro-geometry part surface shape that includes surface roughness, waviness, contour error, texture, etc.) has had increased attention by researchers and manufacturers alike. This is due to the fact that surface topography greatly effects such characteristics as mating of parts, surface wear, lubrication status, fiction, vibration, noise, fatigue, sealing, coating quality, corrosion resistance, electrical conductivity, thermal conductivity, and reflection performance [1, 2]. Therefore, the investigation of the generation and modeling of surface geometric topography is vital for optimizing part performance.

Ball-end milling is a very adaptable process which is widely used in the machining of complicated surfaces, which are often encountered in the aerospace, automotive, and die and mold industries. In conventional machining, complicated surfaces have to be polished, typically using a manual process,

after cutting is complete, which will result in increased processing time and inferior surface quality. Milling with ball-end milling cutter, combining new technologies such as high-speed machining technology, multi-axis control technology, and precision manufacturing technology, could meet the high requirements of surface quality instead of the hand-made. The geometry of ball-end milling cutter teeth, however, is complex, and the engagement area between cutter tooth and part during the milling process varies constantly. So it is difficult to determine the local machined surface area milled by which cutter tooth and which part of it by traditional experimental method, and the most important is that it is much time consuming by this method. Hence, it is necessary to develop a method to efficiently simulate surface topography for ball-end milling operations.

Imani et al. [3–5] investigated milling surface topography simulation using entity modeling and Boolean operation method. This method is effective in the case of conventional milling, in which the feed per tooth is far less than the step over, resulting in residual heights of the milled surface in the feed direction that are far less than the ones in the interval feed direction. However, the ratio of feed per tooth to step over is greater in high-speed milling than conventional milling, and the residual heights of the milled surface in the feed direction have a dramatic impact on surface roughness, so it cannot be neglected. Therefore, the entity modeling and Boolean operation method cannot be used to effectively analyze end milling operation. This motivated the use of the traditional Z-MAP algorithm to model the surface topography in ball-end milling operation.

The traditional Z-MAP algorithm considers the effects of many factors on the surface topography. Firstly, the part is divided into *x*-*y* grid nodes by a meshing operation, and then the *Z*-coordinates of each grid node according to the cutter tooth position during the milling process are calculated, and the *x*-*y*-*z* vectors are used to describe surface topography [6]. Xu et al. [7] proposed a generalized simulation model for milling surface topography and the peripheral milling experiment is used to prove the model. Hu et al. [8] studied the influence rule of tool assembly error on machined surface in peripheral milling process. Omar et al. [9] established a generic and improved model to predict 3D surface topography during peripheral milling operation. Lavernhe et al. [10, 11] investigated on the surface topography obtained by corner rounding milling cutter under multi-axis controlled. And Franco et al. [12] studied the surface topography milled by face milling cutter. Above studies focus on the surface formed by milling cutter with simple teeth (the teeth contour is simple), which give the reference for ball-end milling surface topography simulation.

Yan et al. [13] established ball-end milling surface topography generatation model, which can be extended to consider more complex motion and process errors. Zhao et al. [14] developed a ball-end milling surface topography simulation model considering cutter posture adjustment, and Zhang et al. [11] established a model which considered both tooth wear and cutter inclination. Zeroudi et al. [15] proposed a rebuilt model, which can directly predict surface topography and roughness of an ideal curved surface. Liu et al. [16] developed a system to simulate ball-end milling surface topography and calculate the surface roughness, and this system could be integrated into popular CAM software. Han et al. [17] developed a model which could predict surface topography and surface roughness of complex curved surfaces via ball-end milling.

The traditional Z-MAP algorithm, however, requires the part and the cutting tool to be divided into discrete segments. In order to increase the precision of the simulation results, the segments must be made smaller, which increases the number of points to simulate, but decreases computational efficiency. As a result, research studies were conducted to improve the traditional Z-MAP algorithm. Zhao et al. [18, 19] utilized solid modeling in the traditional Z-MAP algorithm to quickly predict ball-end milling surface topography, similar to many of the studies discussed above; however, the residual heights in the feed direction are ignored, leading to the decreased simulation accuracy.

Bouzakis et al. [20] developed an improved Z-MAP algorithm, BALLMILL algorithm, the cross-section contour of milled surface in the reference plane of the part are approximated by the linear segments. Antoniadis et al. [21, 22] approximated the swept surface unit to four triangles to easily obtain the whole milled surface with ball-end milling cutter. Peng et al. [23] built micro-ball-end milling surface topography by servo bounding boxes and heights of a few crucial points among cutter tooth sweeping point cloud.

However, these improved Z-MAP algorithm can easily cause approximation error. All of the methods mentioned above conduct the computational process according to the unit time interval, in which both the cutter tooth and part are discrete, and the swept part node in the unit time interval is no more than 1, which lead to the computational efficiency and computational accuracy that are hard to trade-off. And the approximation method and neglect of surface residual height in feed direction lead to the simulation error.

This paper proposes an improved Z-MAP algorithm which keeps the advantage of strong extensibility of the time interval controlled, and overcomes the shortage of low precision and efficiency of the traditional Z-MAP algorithm. In the preprocessing of the proposed improved algorithm, the cutter tooth is not discrete, and the swept part node in the unit time interval is not restricted (instead of no more than 1 in traditional Z-MAP). During the computation process, the improved Z-MAP algorithm applies a servo rectangular encirclement, angle summation method, and numerical calculation method to conduct the surface topography simulation. The experimental

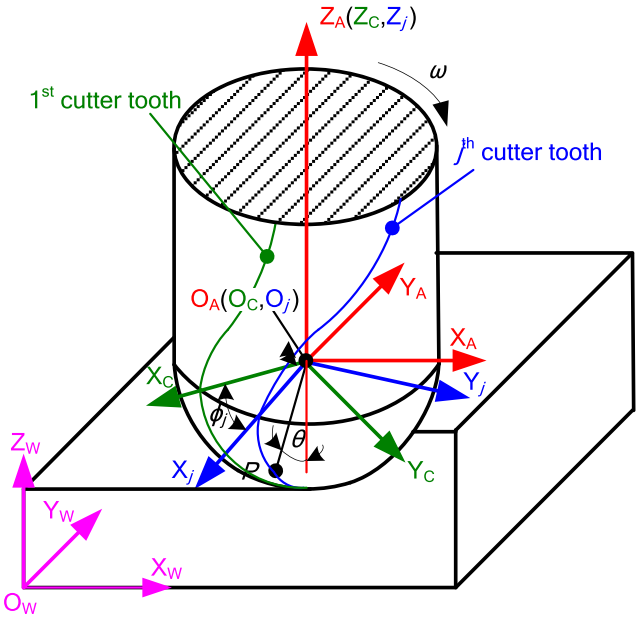

Fig. 1 Reference coordinate systems of cutter tooth trajectory

results demonstrate the effectiveness of the proposed simulation algorithm.

2 Trajectory modeling of ball-end milling cutter teeth

Simulating surface topography in ball-end milling requires the establishment of a trajectory equation for the cutter teeth. The reference coordinate systems are used to describe the trajectory shown in Fig. 1. The coordinate system O_W-$X_WY_WZ_W$, denoted $\{W\}$, is fixed to the part and is known as the work space coordinate system or part coordinate system. The coordinate system O_A-$X_AY_AZ_A$, denoted $\{A\}$, in which the origin O_A coincides with O_C, is the center of sphere part of ball-end milling cutter. X_A-axis and Y_A-axis parallel to X_W-axis and Y_W-axis respectively, which moves with spindle, is called the spindle servo coordinate system. The coordinate system O_C-$X_CY_CZ_C$, denoted $\{C\}$, in which the cutter axis, Z_C, rotates around the spindle axis with angular velocity ω and the X_C-axis is in the direction of the first cutter tooth, is known as the cutter coordinate system. The coordinate system O_j-$X_jY_jZ_j$, denoted $\{j\}$, in which the Z_j-axis and coordinate origin O_j are consistent with the Z_C-axis and coordinate origin O_C, respectively, and the X_j-axis cross the jth cutter tooth, is called cutter tooth coordinate system.

Taking a ball-end milling cutter with planar profile teeth as research object, an arbitrary point P on the jth cutter tooth is

$$\begin{bmatrix} x_{jP} & x_{jP} & x_{jP} & 1 \end{bmatrix}^T = \begin{bmatrix} R\sin(\theta) & 0 & -R\cos(\theta) & 1 \end{bmatrix}^T \quad (1)$$

where θ is the axial immersion angle of the point P (degree), and R is the cutter radius (mm). The transformation from coordinate system $\{C\}$ to coordinate system $\{j\}$ is

$$M_{Cj} = \begin{bmatrix} \cos(\varphi_j) & -\sin(\varphi_j) & 0 & 0 \\ \sin(\varphi_j) & \cos(\varphi_j) & 0 & 0 \\ 0 & 0 & 1 & 0 \\ 0 & 0 & 0 & 1 \end{bmatrix} = \begin{bmatrix} \cos(2\pi(j-1)/n_t) & -\sin(2\pi(j-1)/n_t) & 0 & 0 \\ \sin(2\pi(j-1)/n_t) & \cos(2\pi(j-1)/n_t) & 0 & 0 \\ 0 & 0 & 1 & 0 \\ 0 & 0 & 0 & 1 \end{bmatrix} \quad (2)$$

where φ_j is the included angle between a cutter tooth and the first cutter tooth (degree), and n_t is the number of cutter teeth.

The cutter orientation greatly influences surface topography and, thus, part quality in the milling. For a spindle speed of N (r/min), the cutter coordinate system $\{C\}$ rotates around the negative O_AZ_A-axis with angular velocity $\omega = \pi N/30$ (rad/s). Considering the rotation of the spindle and the cutter orientation, the homogeneous transformation matrix from coordinate system $\{A\}$ to $\{C\}$ is

$$M_{AC} = \begin{bmatrix} \cos(\tau)\cos(\beta) & -\sin(\tau)\cos(\beta) & \sin(\beta) & 0 \\ \sin(\alpha)\sin(\beta)\cos(\tau) + \sin(\tau)\cos(\alpha) & -sin(\alpha)\sin(\beta)\sin(\tau) + \cos(\alpha)\cos(\tau) & -\sin(\alpha)\cos(\beta) & 0 \\ -cos(\alpha)\sin(\beta)\cos(\tau) + \sin(\tau)\sin(\alpha) & \cos(\alpha)\sin(\beta)\sin(\tau) + \sin(\alpha)\cos(\tau) & \cos(\alpha)\cos(\beta) & 0 \\ 0 & 0 & 0 & 1 \end{bmatrix} \quad (3)$$

$$\tau = A_i - \frac{180\omega t}{\pi}$$

where A_i, as shown in Fig. 2, is the initial phase angle between the first cutter tooth and feed path (degree). t is time (s), and α (degree) and β (degree), shown in Fig. 3, are the cutter lead angle (the rotation of the tool axis on the cutter interval feed direction axis, X-axis) and the cutter tilt angle (the rotation about the cutter feed direction axis, Y-axis), respectively. Here counterclockwise is defined as positive.

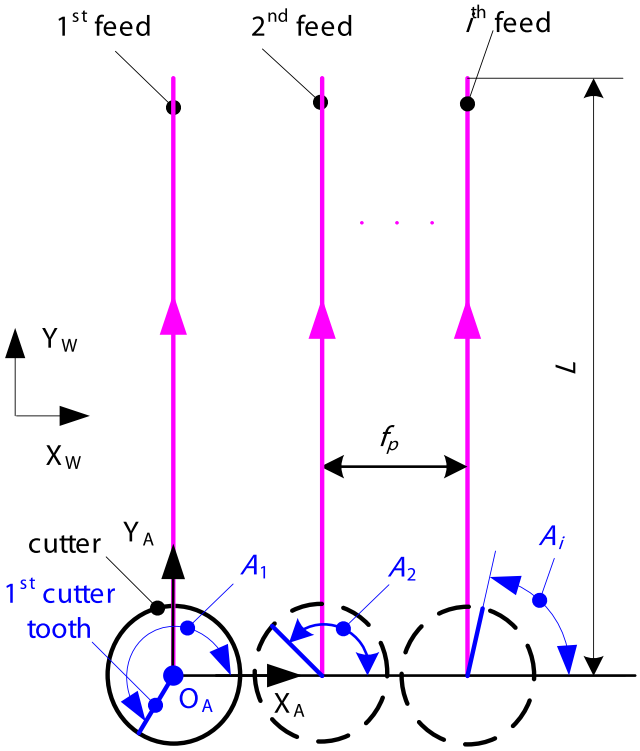

Fig. 2 One-way motion trajectory of ball-end milling cutter

The cutter feeds along the *Y*-axis, the *X*-axis is the interval feed direction. The initial cutter location of O_C during the first feed path in the part coordinate system $\{W\}$ is (x_0, y_0, z_0). Then, in the feed paths as shown in Fig. 3, ignoring the time

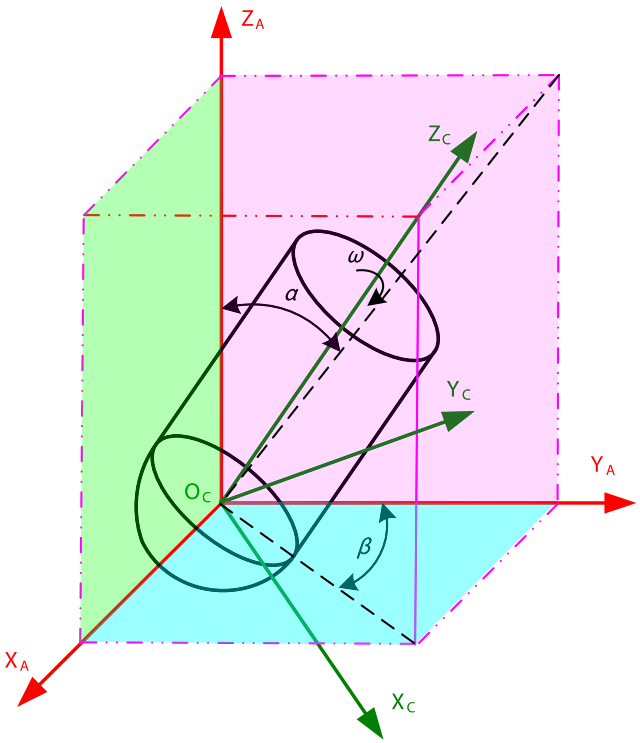

Fig. 3 Cutter orientation

moving from one path to another, the homogeneous transformation from the part coordinate system $\{W\}$ to the spindle coordinate system $\{A\}$ is

$$M_{\mathrm{WA}} = \begin{bmatrix} 1 & 0 & 0 & x_0 + (i-1)f_p \\ 0 & 1 & 0 & y_0 + \dfrac{Nn_t f_f t}{60} - L \\ 0 & 0 & 1 & z_0 \\ 0 & 0 & 0 & 1 \end{bmatrix} \tag{4}$$

where i is the cutter path ($i = 1, 2, 3,$), f_f is cutter feed per tooth (mm/r), f_p is the step over distance (mm), and L is the length of every feed path (mm).

After the coordinate transformation, the trajectory of an arbitrary point P on the cutter tooth in the part coordinate system $\{W\}$ is

$$\left[x_{wp}(t,\theta), y_{wp}(t,\theta), z_{wp}(t,\theta), 1\right]^{\mathrm{T}} = M_{\mathrm{WA}} M_{\mathrm{AC}} M_{\mathrm{C}j} \left[x_{jp}, y_{jp}, z_{jp}, 1\right]^{\mathrm{T}} \tag{5}$$

3 Modeling of ball-end milling surface topography based on the improved Z-MAP algorithm

The traditional Z-MAP algorithm divides part into *x*-*y* grid nodes by meshing operation and then calculates the *Z*-coordinates of each node according to the cutter tooth position in milling process. The modeling of ball-end milling surface topography is to calculate the part height coordinates (i.e., *Z*-coordinates) at discrete locations (i.e., *X* and *Y* coordinates) swept by a cutter tooth using Eq. (5). Part height coordinate algorithm is:

Step 1. Initialization, which sets: (1) the cutter parameters, such as ball-end mill cutter radius R and number of cutter tooth n_t. (2) Blank dimension (i.e., part dimension before milling) and discrete model. The blank dimension is set to $l_x \times l_y \times h_z$ and is divided into $m \times n$ discrete grids in the $X_W O_W Y_W$ plane according to Eq. (6) in order to keep the precision of calculation later.

$$\max\left(\frac{l_x}{n}, \frac{l_y}{m}\right) \le \frac{1}{10}\min\left(f_f, f_p\right) \tag{6}$$

The part upper surface height (*Z*-coordinate) of each grid node, as shown in Fig. 4, is saved in the matrix $Z\,[ii,jj]$ ($ii = 1, 2,\ldots m+1$; $jj = 1, 2,\ldots n+1$), and the initial values of all of the elements of the matrix Z are the blank height, h_z (mm). (3) Milling parameters, which include spindle speed N, feed per tooth f_f, depth of cut a_p (this paper does not discuss since it has little effect on the surface topography under finish milling), and step over f_p. (4) Cutter orientation, which includes the lead angle α and the tilt angle β. Based on the parameters set up,

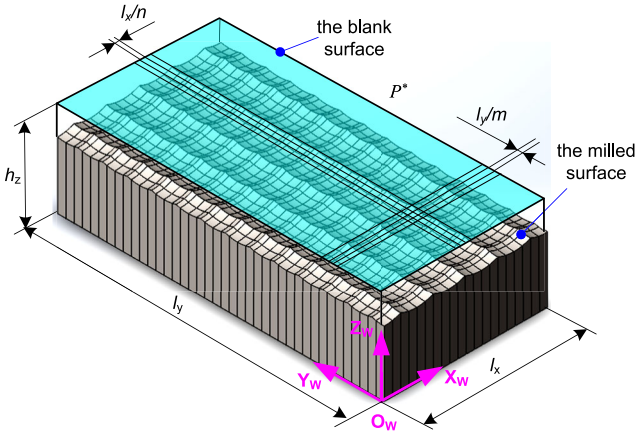

Fig. 4 Discrete model of part

the spending time that the cutter rotates 10° to 20° is considered as time interval Δt [21, 22], unlike the traditional Z-MAP algorithm, in which there is at most one grid point that can be swept by cutter during unit time interval.

Also, unlike traditional Z-MAP algorithm, the cutter tooth need not to be dispersed since the corresponding point of the cutter tooth which swept instantaneously the grid nodes of the part is solved by Newton iterative algorithm in the improved Z-MAP algorithm. (5) Current cutting time $t = 0$, the number of cutter tooth $j = 1$, which is benchmark cutter tooth.

Step 2. Determination of cutter tooth encirclement. The rectangle that encircles the cutter tooth, which includes all points swept instantaneously, is shown in Fig. 5. The ball-end milling cutter's radius R, cutting depth a_p, lead angle α, and tilt angle β are shown in Fig. 6.

The cutter inclination angle A_t means the included angle of part axis Z_W and tool axis Z_C. From Fig. 1, the relationship between A_t and α and β is

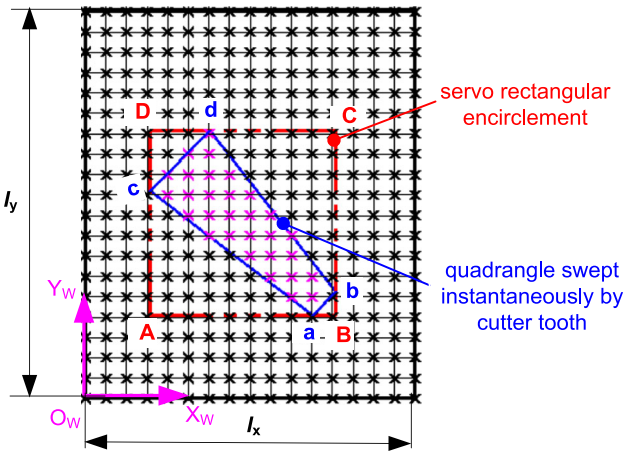

Fig. 5 Part grid nodes showing cutter tooth encirclement and quadrangle sweet by cutter tooth

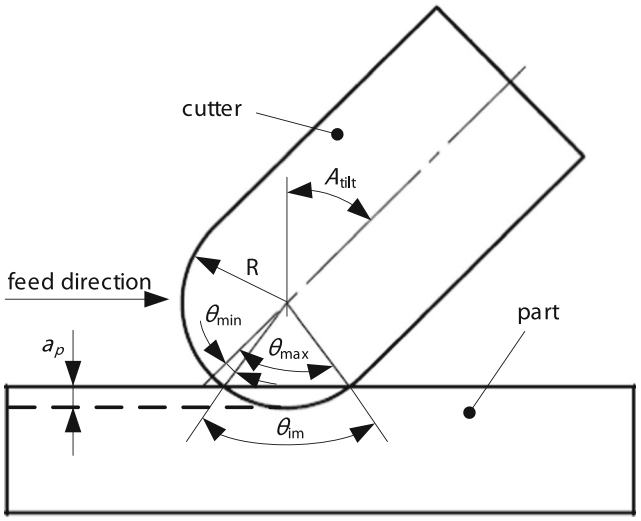

Fig. 6 Working state of ball-end milling cutter

$$A_t = \arccos(\cos(\alpha)\cos(\beta)) \tag{7}$$

The axial immersion included angle θ_{im} (i.e., angular range from initial axial immersion angle $\theta_{\min}$ to terminal axial immersion angle $\theta_{\max}$), which is

$$\theta_{im} = 2\arccos((R - a_P)/R) \tag{8}$$

The initial axial immersion angle $\theta_{\min}$ and terminal axial immersion angle $\theta_{\max}$ are solved according to Eqs. (9) and (10), respectively. However, if $\theta_{\min} \le 0°$, $\theta_{\min} = 0°$, and if $\theta_{\max} \ge 90°$, $\theta_{\max} = 90°$.

$$\theta_{\min} = A_t - 0.5\theta_{im} \tag{9}$$

$$\theta_{\max} = A_t + 0.5\theta_{im} \tag{10}$$

Set $P_x(r, j, s)$ is the coordinate value in X-axis, r means cutting moment, $r = 1, 2$, $r = 1$ means the current cutting moment, and $r = 2$ means the next cutting moment. The j means the jth cutter tooth, and s represents the immersion angle, $s = 1, 2$, $s = 1$ means $\theta = \theta_{\min}$, and $s = 2$ means $\theta = \theta_{\max}$. $P_y(r, j, s)$ and $P_z(r, j, s)$ are the coordinate values in Y- and Z-axes, respectively. Based on Eq. (5), the coordinates of two swept part grid points $[P_x(1, j, 1), P_y(1, j, 1), P_z(1, j, 1)]$ and $[P_x(1, j, 2), P_y(1, j, 2), P_z(1, j, 2)]$ corresponding to points on the jth cutter tooth with axial immersion angles $\theta_{\min}$ and $\theta_{\max}$, respectively, at the current sampling time t, respectively, are

$$\begin{bmatrix} P_x(1,j,1) \\ P_y(1,j,1) \\ P_z(1,j,1) \\ 1 \end{bmatrix} = \begin{bmatrix} x_{WP}(t,\theta_{\min}) \\ y_{WP}(t,\theta_{\min}) \\ z_{WP}(t,\theta_{\min}) \\ 1 \end{bmatrix} \tag{11}$$

$$\begin{bmatrix} P_x(1,j,2) \\ P_y(1,j,2) \\ P_z(1,j,2) \\ 1 \end{bmatrix} = \begin{bmatrix} x_{WP}(t,\theta_{\max}) \\ y_{WP}(t,\theta_{\max}) \\ z_{WP}(t,\theta_{\max}) \\ 1 \end{bmatrix} \tag{12}$$

Correspondingly, the coordinates of two swept part grid points $[P_x(2, j, 1), P_y(2, j, 1), P_z(2, j, 1)]$ and $[P_x(2, j, 2), P_y(2, j, 2), P_z(2, j, 2)]$ on the next sampling time $t + \Delta t$ are

$$\begin{bmatrix} P_x(2,j,1) \\ P_y(2,j,1) \\ P_z(2,j,1) \\ 1 \end{bmatrix} = \begin{bmatrix} x_{WP}(t+\Delta t, \theta_{\min}) \\ y_{WP}(t+\Delta t, \theta_{\min}) \\ z_{WP}(t+\Delta t, \theta_{\min}) \\ 1 \end{bmatrix} \quad (13)$$

$$\begin{bmatrix} P_x(2,j,2) \\ P_y(2,j,2) \\ P_z(2,j,2) \\ 1 \end{bmatrix} = \begin{bmatrix} x_{WP}(t+\Delta t, \theta_{\max}) \\ y_{WP}(t+\Delta t, \theta_{\max}) \\ z_{WP}(t+\Delta t, \theta_{\max}) \\ 1 \end{bmatrix} \quad (14)$$

The $x_{\min}$ and $x_{\max}$ are the minimum and maximum in the X-direction coordinates among four points $[P_x(1, j, 1)]$, $[P_x(1, j, 2),]$, $[P_x(2, j, 1)]$, and $[P_x(2, j, 2)]$, respectively. The $y_{\min}$ and $y_{\max}$ are the minimum and maximum in the Y-direction coordinates among four points $[P_y(1, j, 1)]$, $[P_y(1, j, 2),]$, $[P_y(2, j, 1)]$, and $[P_y(2, j, 2)]$, respectively.

The rectangular boundary of the jth cutter tooth during a sampling interval is shown in Fig. 5. The four edges of rectangular are A ($x_{\min}$, $y_{\min}$), B ($x_{\max}$, $y_{\min}$), C ($x_{\max}$, $y_{\max}$), and D ($x_{\min}$, $y_{\max}$).

Step 3. Establishing the quadrangle area swept instantaneously by cutter tooth and the grid points that fall into this area. In Fig. 5, taking the four points: a$[P_x(1, j, 1), P_y(1, j, 1)]$, b$[P_x(2, j, 1), P_y(2, j, 1)]$, c$[P_x(1, j, 2), P_y(1, j, 2)]$, and d$[P_x(2, j, 2), P_y(2, j, 2)]$ calculated from Step 2, the algorithm determines the quadrangle area swept instantaneously by the cutter tooth. An algorithm is used to search for the grid points in the rectangular boundary. The included angle $Angle_k$ (shown in Fig. 7) is between two lines which are from two different adjacent points of the swept quadrangle to searched grid point

$$Angle_k = \arccos\left(\frac{(P_{x^*}-P_{x\_mm})(P_{x^*}-P_{x\_nn}) + (P_{y^*}-P_{y\_mm})(P_{y^*}-P_{y\_nn})}{\sqrt{(P_{x^*}-P_{x\_mm})^2 + (P_{y^*}-P_{y\_mm})^2}\sqrt{(P_{x^*}-P_{x\_nn})^2 + (P_{y^*}-P_{y\_nn})^2}}\right) \quad (16)$$

where $Angle_k$ is less than or equal to 180°. $P_{mm}(P_{x\_mm}, P_{y\_mm})$ and $P_{nn}(P_{x\_nn}, P_{y\_nn})$ are adjacent points, and $\{(P_{x\_mm}, P_{y\_mm}), (P_{x\_nn}, P_{y\_nn})\} \in \{(P_x(1,j,1), P_y(1,j,1)), (P_x(2,j,1), P_y(2,j,1)), (P_x(2,j,2), P_y(2,j,2)), (P_x(1,j,2), P_y(1,j,2))\}$, $k = 1, 2, 3, 4$. $P^*(P_{x^*}, P_{y^*})$ is the grid point. For example, the $Angle_1$ in Fig. 7 is,

$$Angle_1 = \arccos\left(\frac{(P_{x^*}-P_x(1,j,1))(P_{x^*}-P_x(2,j,1)) + (P_{y^*}-P_y(1,j,1))(P_{y^*}-P_y(2,j,1))}{\sqrt{\left((P_{x^*}-P_x(1,j,1))^2 + (P_{y^*}-P_y(1,j,1))^2\right)\left((P_{x^*}-P_x(2,j,1))^2 + (P_{y^*}-P_y(2,j,1))^2\right)}}\right)$$

The angle summation shown in Fig. 7 is used to determine if a grid point $P^*(P_{x^*}, P_{y^*})$ is within the rectangular boundary that lies in the instantaneously swept quadrangle, that is, if $|Angle_1 + Angle_2 + Angle_3 + Angle_4 - 360| = 0$. The grid point $P^*(P_{x^*}, P_{y^*})$ is out of the instantaneously swept quadrangle, if $(Angle_1 + Angle_2 + Angle_3 + Angle_4 - 360) < 0$.

Step 4. Calculating the height coordinate of part grid points within the swept quadrangle. After calculating the coordinate $P^*(P_{x^*}, P_{y^*})$ of a part grid point within the swept quadrangle, the cutting time t and immersion angle θ at which the cutter tooth intersects the grid point are determined. Converting the first two items of Eq. (5), which is

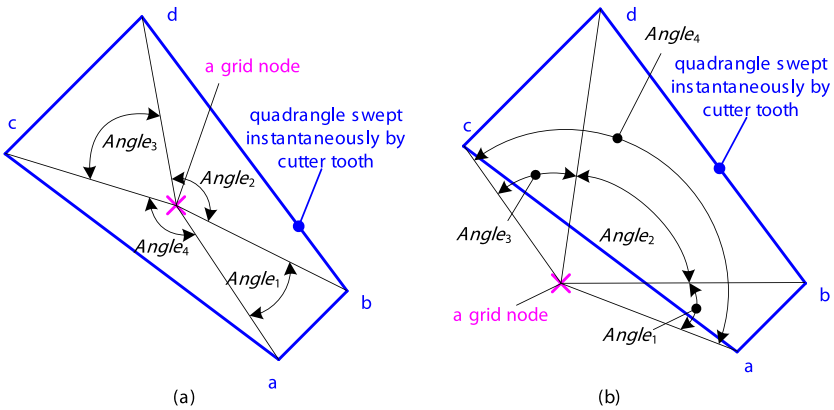

Fig. 7 Schematic diagram of angle summation method. **a** Grid point is inside of instantaneously swept quadrangle and **b** grid point is outside of instantaneously swept quadrangle

$$f_x(t,\theta) = x_{wp}(t,\theta) - P_{x^*} = 0$$
$$f_y(t,\theta) = y_{wp}(t,\theta) - P_{y^*} = 0 \tag{17}$$

The Newton-Raphson method is used to solve Eq. (17),

$$\begin{bmatrix} t_k \\ \theta_k \end{bmatrix} = \begin{bmatrix} t_{k-1} \\ \theta_{k-1} \end{bmatrix} - \begin{bmatrix} \frac{\partial f_x}{\partial t} & \frac{\partial f_x}{\partial \theta} \\ \frac{\partial f_y}{\partial t} & \frac{\partial f_y}{\partial \theta} \end{bmatrix}^{-1} \begin{bmatrix} f_x(t_{k-1},\theta_{k-1}) \\ f_y(t_{k-1},\theta_{k-1}) \end{bmatrix} \tag{18}$$

where $\begin{bmatrix} t_0 \\ \theta_0 \end{bmatrix} = \begin{bmatrix} T - 0.5\Delta t \\ 0.5(\theta_{\min} + \theta_{\max}) \end{bmatrix}$ are the initial values, and the convergence accuracy is set to $\begin{bmatrix} t_k - t_{k-1} \\ \theta_k - \theta_{k-1} \end{bmatrix} = \begin{bmatrix} 0.00001 \\ 0.001 \end{bmatrix}$. Substituting the result of Eq. (18) into Eq. (5), the height coordinate of swept point is

$$z_{wp}{}^* = z_{wp}(t_k, \theta_k) \tag{19}$$

Step 5. Determining whether or not the part grid point is cut. If $z_{wp0} < Z(ii, jj)$, i.e., the cutter cuts the part, then $Z(ii, jj) = z_{wp0}$. Otherwise, keep the current value of matrix element $Z(ii, jj)$.

Steps 4 and 5 are repeated for every point in the quadrangle. In the current time step, the relevant the calculation of the next cutter tooth is carried out by repeating Steps 2–5, until the final cutter tooth is done. Then, turning to the next time step, the cutter is indexed to the next location and Steps 2 and 3 are repeated. This sequence is repeated until the cutter has cleared the part.

4 Simulating the process parameter influence on surface topography

Process parameters such as step over f_p, feed per tooth f_f, lead angle α, tilt angle β, and the initial phase angle difference of the first cutter tooth ΔA greatly influence part surface topography in ball-end milling operations. Each process parameter is analyzed individually to determine its influence on part surface topology. The initial phase angle difference of the first cutter tooth in different feed paths is

$$\Delta A = A_{i+1} - A_i \tag{20}$$

where A_i is the initial phase angle at the beginning of the ith feed path, and $i = 1, 2, 3, \ldots$ and is shown in Fig. 8. A monolithic carbide ball-end milling cutter, diameter of 10 mm with two plane teeth, is used in the simulation. The maximum height S_y, the distance between the highest and the lowest points on the surface within the evaluation area D which is used to characterize the milled surface, is

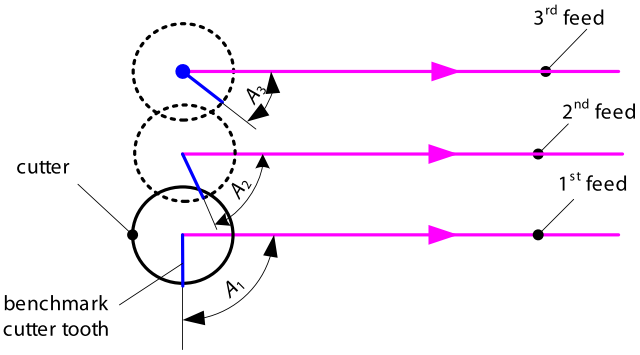

Fig. 8 Schematic of cutter tooth initial phase angle

$$S_y = |z(x,y)|_{peak} - z(x,y)|_{valley}|_{(x,y)\in D}$$
$$= \left| z\left(x_{ii}, y_{jj}\right)\right|_{peak} - z\left(x_{ii}, y_{jj}\right)|_{valley} \Big| \begin{matrix} 1 \le ii \le m+1 \\ 1 \le jj \le n+1 \end{matrix} \tag{21}$$

where $(x_{ii}, y_{jj}) \in D$, and $ii = 1, 2, \ldots, m+1; jj = 1, 2, \ldots, n+1$.

In order to obtain the influence of feed per tooth f_f on ball-end milling surface topography, the ratio between feed per tooth and step over, f_f/f_p, is set to 0.1, 0.2, 0.3, …, 2.0 when step over is 0.25, 0.50, and 0.75 mm, respectively, and other parameters are $a_p = 0.5$ mm, $N = 3000$ rpm, $\alpha = 0°$, $\beta = 0°$, and $\Delta A = 0°$, respectively. Figure 9 shows the influence of feed per tooth on surface topography.

Figure 10 shows S_y increases with the increase of ratio of f_f/f_p, and the increasing rate is slow when $f_f/f_p < 0.65$ and $f_f/f_p > 1.08$ [24]; however, it changes rapidly in the period ($0.65 \le f_f/f_p \le 1.08$). Figure 10 shows that the maximum residual heights of surface locate in planes which coordinate $y_w = Mf_f$ ($M = 1, 2, \ldots$), M is and on the intersecting curve of two swept surfaces formed by the trajectories of adjacent cutter teeth in the ith feed, and also perhaps in the $(i-1)$th feed in this cutting condition that $\Delta A = 0°$. In order to solve S_y, the formation of the maximum residual height is classified in three cases shown in section I-I in Fig. 10. The curves $C_{R,i}$ and $C_{L,i}$ represent intersecting curve formed by right side of the trajectories of adjacent cutter teeth in the ith feed and by left side of the trajectories of adjacent cutter teeth in the ith feed, respectively, and so on. According to the literature [24], S_y is

$$S_y = R - \sqrt{R^2 - R_{eff}{}^2} \tag{22}$$

where R_{eff} is the radius of sweeping point on the cutter tooth when it is just across the point corresponding to the maximum residual height, and it is different in three cases.

In case I:

$$R_{eff} = f_f\left(\frac{\lambda_1}{\pi}\right) sec(\lambda_1) \tag{23}$$

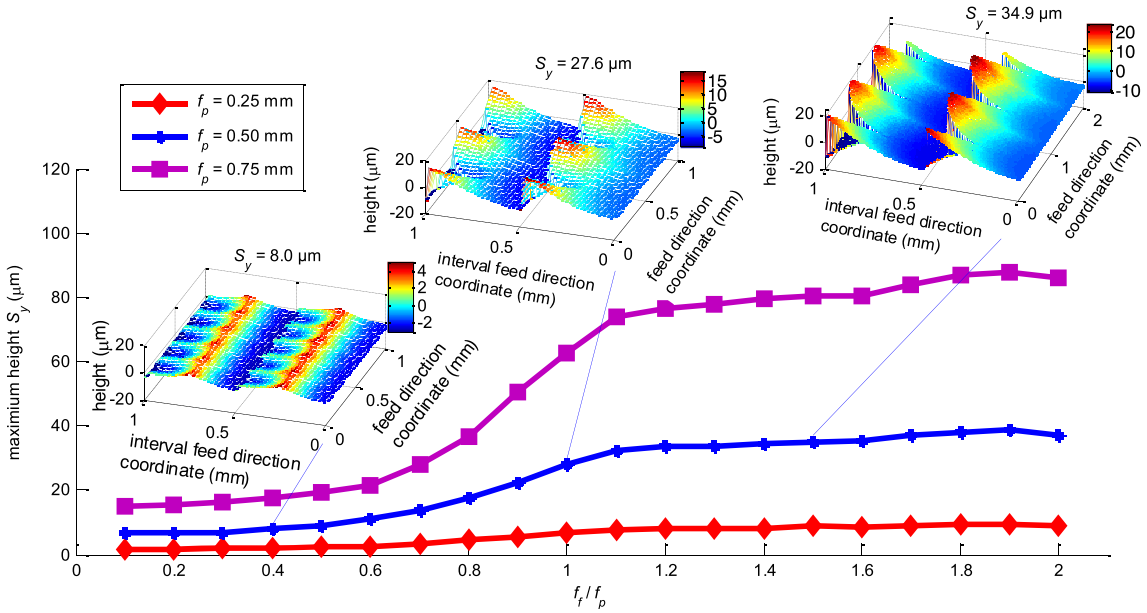

Fig. 9 Influence of feed per tooth on surface topography with the depth of cut 0.5 mm, step over 0.5 mm, spindle speed 3000 rpm, cutter lead angle 0°, tilt angle 0°, and the initial phase angle difference of cutter tooth 0°

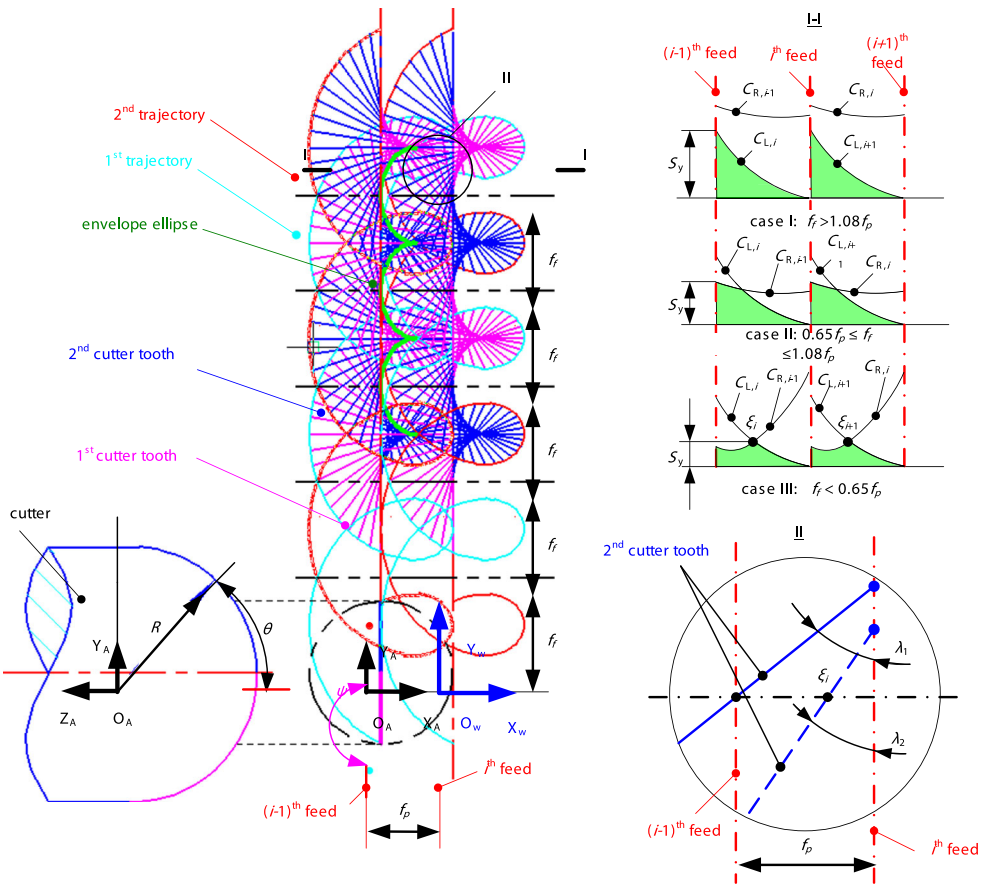

Fig. 10 The formation mechanism of maximum residual height of ball-end milling surface topography

In case II:

$$R_{eff} = f_f \tag{24}$$

In case III:

$$R_{eff} = f_f \left(\frac{\lambda_2}{\pi}\right) sec(\lambda_2) \tag{25}$$

In cases I and III, λ_1 and λ_2 decrease with the increase of f_f, so that the increasing rate of R_{eff} is slow, this is because the increasing rates of S_y are different in the different periods of f_f/f_p. In order to determine the step over f_p influence on ball-end milling surface topography, a set of simulations are conducted with $f_p = 0.1, 0.2, \ldots, 1.0$ mm under the different feeds per tooth $f_f = 0.2$, 0.4, and 0.6 mm. The α, β, and ΔA are 0.2 mm/r, 0°, and 0°, respectively.

From Fig. 11, S_y increases with step over f_p increasing, but the increasing rates at different f_p are different. The three cases are:

Case I. $f_p < 0.93 f_f$
Case II. $0.93 f_f < f_p < 1.54 f_f$
Case III. $f_p > 1.54 f_f$

When f_p corresponds to case II, as Fig. 11 shows, S_y changes a little; when it is corresponding to the other cases, λ_1 or λ_2 in (23) or (25) is greater when f_p is increased, so that S_y increases with the increase of f_p. In order to examine how the tilt angle β influences the surface topography, simulations are conducted with $\beta = -35°, -30°, -25°, \ldots, 35°$. The other parameters f_p, f_f, α, and ΔA_i are 0.5 mm, 0.2 mm/r, 0°, and 0°, respectively.

Figure 12 illustrates how the tilt angle β influences S_y and the 3D surface topographies. From Fig. 12, S_y is large when $\beta \in (-10°, 5°)$, and reaches a maximum when $\beta = 0°$, but it decreases with the increase of absolute value of β when $\beta \in (-35°, -10°)$, and it is near constant when $\beta \in (5°, 35°)$.

S_y of surface obtained by tilting cutter with positive angle is slightly greater than with the negative, for that tilting cutter with positive angle is down milling and tilting cutter with negative angle is up milling. From Fig. 13, down milling lead to the greater residual height than up milling in the same condition from geometric relationship of trajectories of cutter teeth. The minimum effective radius (the active cutting radius) of ball-end cutter teeth directly affects the maximum residual height of surface; the smaller the radius is, the larger the S_y is. The minimum effective radius is decreasing with the decreasing of tilted angle, hence a largest S_y at zero of tilt angle. In the same time, the residual heights of the milled surface in the feed direction are higher when $\beta = 0°$; however, it is lower when $\beta = -30°$ or 30°, which leads to the total residual heights' decrease.

In order to determine how the cutter lead angle α influences the surface topography, simulation studies are conducted with $\alpha = -35°, -30°, -25°, \ldots, 35°$. The other parameters f_p, f_f, β, and ΔA_i are 0.5 mm, 0.2 mm/r, 0°, and 0°, respectively. Figure 14 shows that cutter lead angle α influences S_y and 3D surface topographies for $-30 \le \alpha \le 30°$. From Fig. 14, the curve is basically symmetric about the straight line of $\alpha = 0°$, S_y is greater when $\alpha \in (-5°, 5°)$, and it reaches to

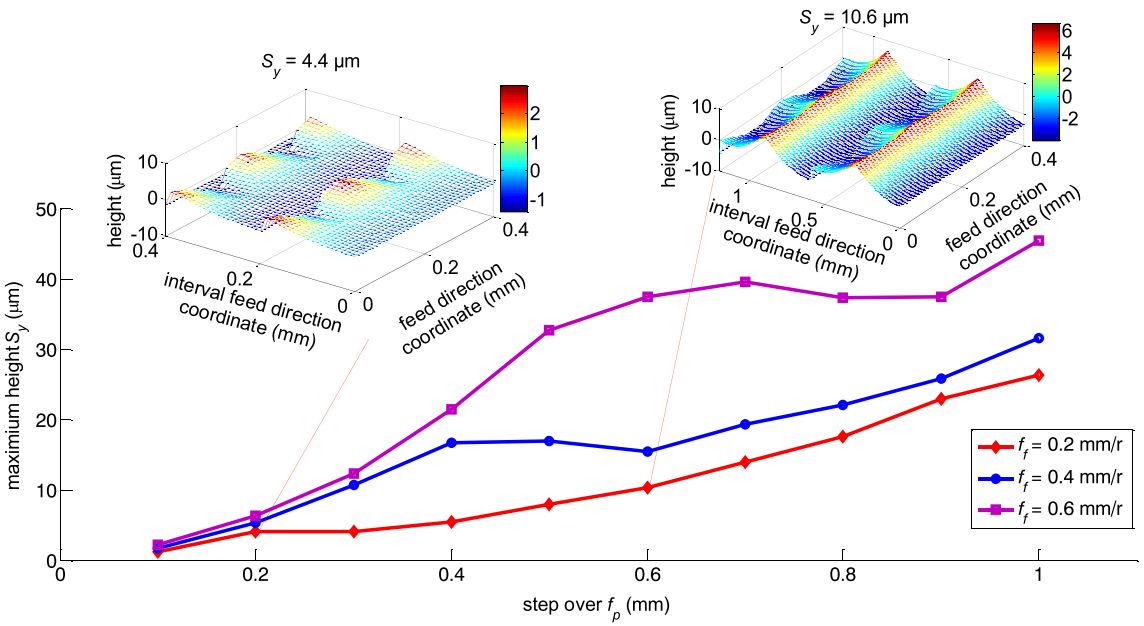

Fig. 11 Influence of step over on surface topography with the depth of cut 0.5 mm, feed per tooth 0.2 mm, spindle speed 3000 rpm, cutter lead angle 0°, tilt angle 0°, and the initial phase angle difference of cutter tooth 0°

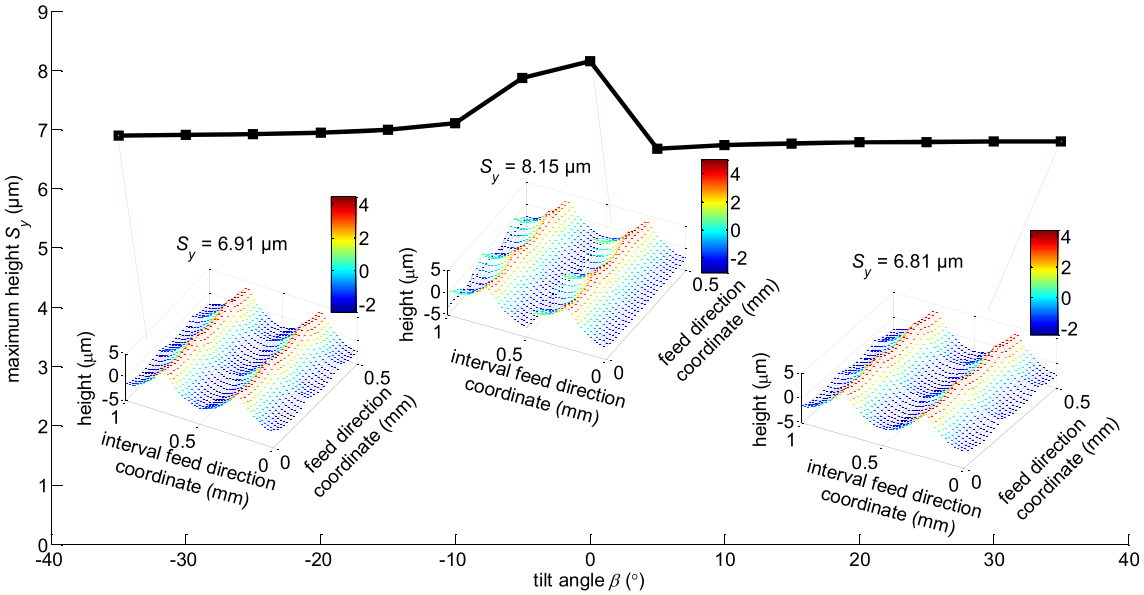

Fig. 12 Influence of cutter tilt angle on surface topography with the depth of cut 0.5 mm, step over 0.5 mm, feed per tooth 0.2 mm, spindle speed 3000 rpm, cutter lead angle 0°, and the initial phase angle difference of cutter tooth 0°

the summit when $\alpha = 0°$, and it decreases with the increase of the α within $\alpha \in (-15°, -5°)$ or $\alpha \in (5°, 15°)$, but it is basically the same when α is out of the two ranges. Similarly to the influence of tilt angle β on surface topography, the residual height of surface milled in the feed direction is the highest while $\alpha = 0°$, it is lower when $\alpha = -30°$ or 30°, and lead to the total surface roughness decrease.

In order to determine the influence of cutter tooth initial phase angle difference ΔA on the surface topography, simulation studies are conducted with $\Delta A = 0°, 10°, 20°, \ldots, 170°$. The other parameters f_p, f_f, α, and β are 0.5 mm, 0.2 mm/r, 0°, and 0°, respectively. The simulation results in Fig. 15 show how ΔA influences S_y and 3D surface topographies when $30° \le \Delta A \le 150°$. From Fig. 15, S_y changes with ΔA according to parabolic shape and reaches maximum and minimum when ΔA is equal to 0° and 90°, respectively. The reason is the positions of the maximum residual summits in previous feed are the position of the deepest valley milled in current feed when ΔA is 90°, i.e., the maximum residual height of surface milled of the previous feed is just cut in the current feed; however, it is opposite when ΔA is 0°. S_y has a local inflection point when ΔA is equal to 50° and 130°, respectively.

5 Experimental validation

Ball-end milling experiments using an NC milling center (MC-50) from Haas Automation company are conducted to validate the improved Z-MAP algorithm. The part material is

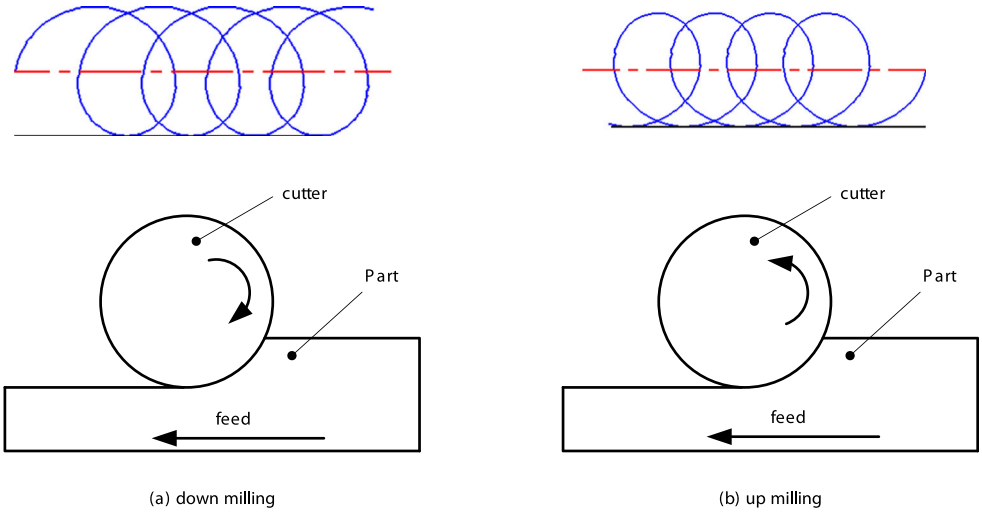

Fig. 13 **a** Down milling and **b** up milling

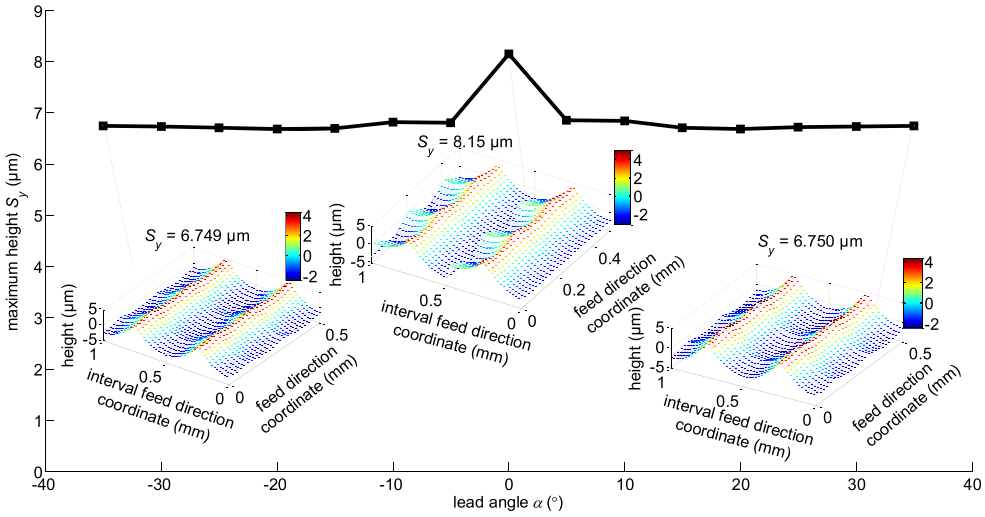

Fig. 14 Influence of cutter lead angle on surface topography with the depth of cut 0.5 mm, step over 0.5 mm, feed per tooth 0.2 mm, spindle speed 3000 rpm, cutter tilt angle 0°, and the initial phase angle difference of cutter tooth 0°

aluminum alloy 7050-T6, and the ball-end milling cutter is made of monolithic carbide with two plane teeth and a 10-mm diameter. Leica DCM-3D with a resolution of 0.1 nm is used to measure surface topography.

Vertical and inclination milling experiments are conducted to validate the improved Z-MAP algorithm. Apart from the 3D surface topography, corresponding 2D section profiles, in both feed and interval feed directions, are investigated. The arithmetic average deviation of contour height, R_a, is used to evaluate the surface roughness, and the root mean square error (*RMSE*) is used to evaluate surface accuracy

$$RMSE = \sqrt{\frac{\sum_{i=1}^{n_P}(Z_{si}-Z_{ei})^2}{n_P}} \tag{26}$$

where Z_{si} and Z_{ei} are the height coordinates of the corresponding sampling points from the simulation and experimental, respectively, and n_P is the number of measured points.

The processing time is used to compare the efficiency of the traditional and improved Z-MAP algorithms. The part is discretized into units with dimension 0.02 × 0.02 mm^2 and the computational iteration error is set to 0.01 μm in simulation. The experiments include vertical milling and inclination milling.

In vertical milling, the machining parameters step over f_p, feed per tooth f_f, cutting depth a_p, spindle speed N, lead angle α, tilt angle β, and cutter tooth initial phase angle difference ΔA_i are set to 0.6 mm, 0.2 mm, 0.5 mm, 3000 r/min, 0°, 0°, and 0°, respectively. Figure 16a–c shows the surface topographies from experiment, simulated by improved and traditional

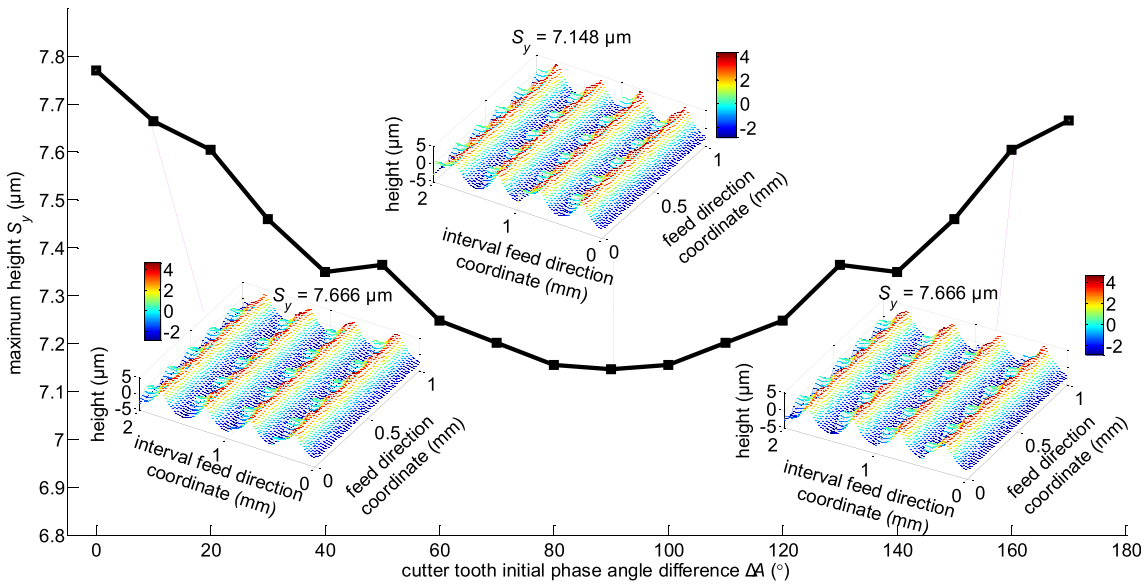

Fig. 15 Influence of cutter tooth initial phase angle difference on surface topography with the depth of cut 0.5 mm, step over 0.5 mm, feed per tooth 0.2 mm, spindle speed 3000 rpm, cutter lead angle 0°, and tilt angle 0°

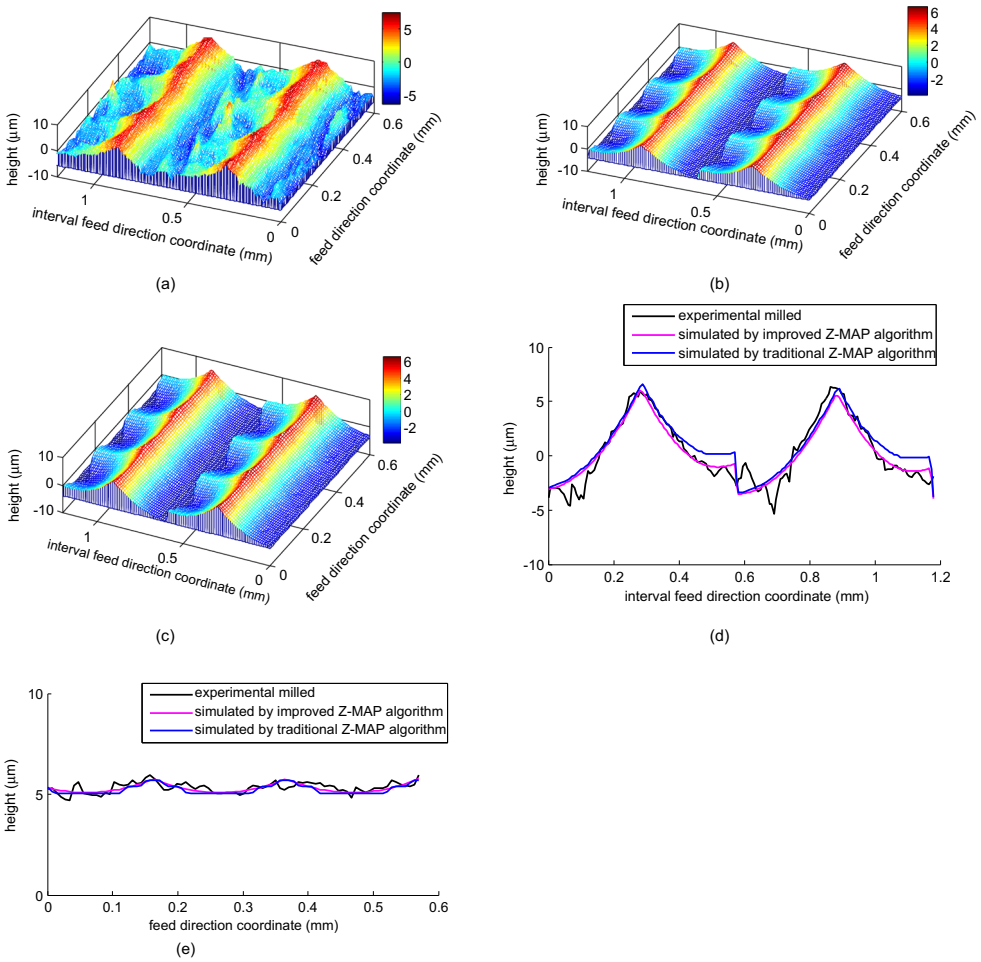

Fig. 16 Comparison between simulated and experimental surface topographies in vertical milling. **a** Surface topography from experimental. **b** Surface topography simulated by improved Z-MAP algorithm. **c** Surface topography simulated by traditional Z-MAP algorithm. **d** Comparison of section profiles in interval feed direction. **e** Comparison of section profiles in feed direction

Z-MAP algorithm, respectively. Figure 16d, e shows the comparison of section profiles in interval feed direction and feed direction. The comparison of R_a and *RMSE* in interval feed and feed directions for the vertical machining operation is in Table 1.

Figure 16a shows the difference of surface topography in the valley between simulations (traditional and improved Z-MAP algorithms) and experiments, that is, in the experiment, the surface of valley is machined by the cutter bottom where the cutting velocity is relatively low and leads to the surface material of the valley plastic deformation which the simulations do not consider. From Table 1 and Fig. 16d, the surface roughness in the interval feed direction between the simulation and experimental is consistent.

The errors between traditional Z-MAP simulation and experiment are bigger than the one between improved Z-MAP simulation and experiment, because the traditional Z-MAP simulations use the approximate method; the calculation of height coordinates of part grid points in traditional Z-MAP algorithm is in Fig. 17. The grid point Q_ε is close to point c among points a, b, c, and d in $X_wO_wY_w$ plane, Q_ε^* and c^* are the points responding to the grid points Q_ε and c in the swept

Table 1 R_a and *RMSE* in interval feed and feed directions for vertical milling simulations and experiment

Method		Experiment	Simulation		Error	
			Traditional Z-MAP	Improved Z-MAP	Traditional Z-MAP	Improved Z-MAP
Feed direction	R_a (μm)	0.2	0.17	0.18	15%	10%
	RMSE (μm)		0.04	0.03		
Interval feed direction	R_a (μm)	2.6	2.21	2.35	15%	9.6%
	RMSE (μm)		0.09	0.07		

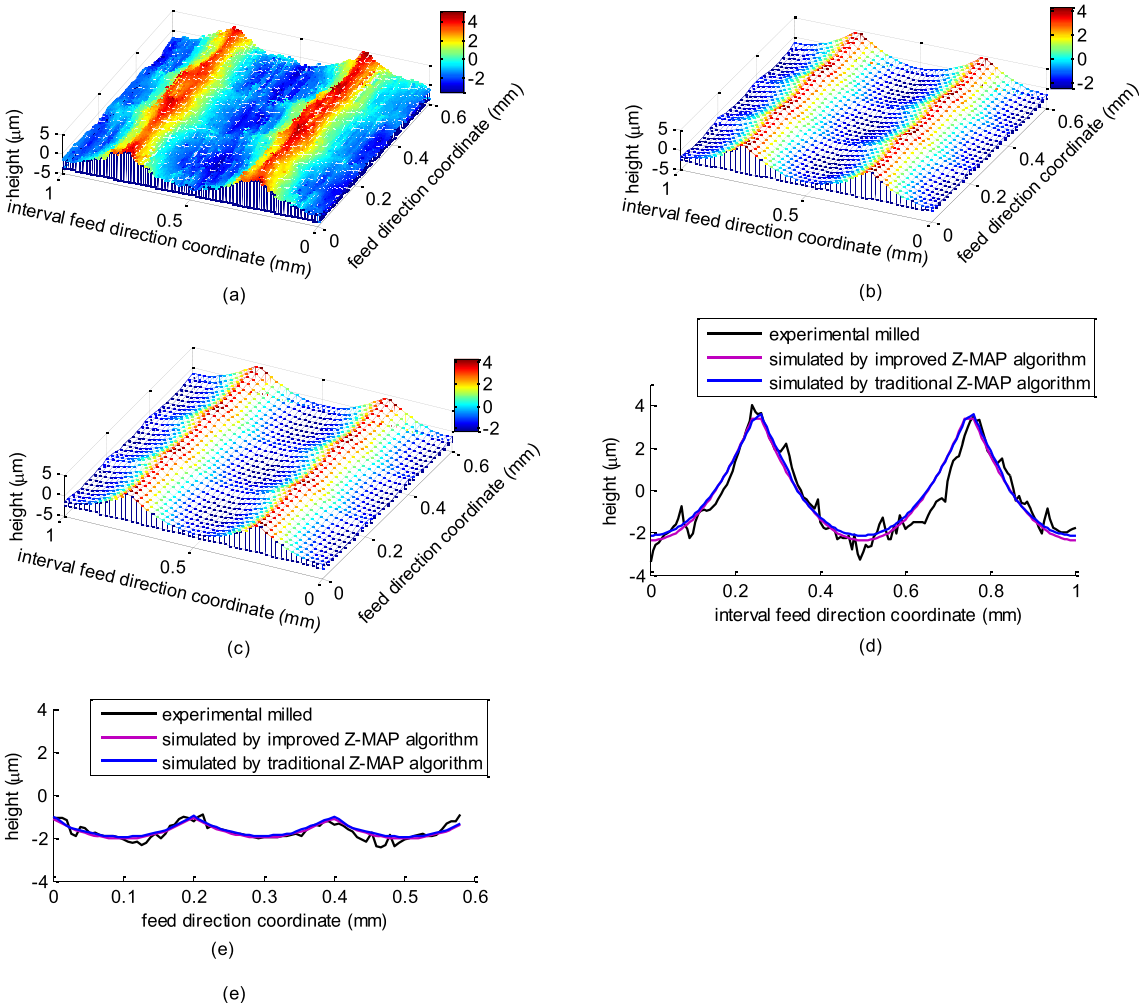

Fig. 17 Comparison surface topographies between simulated and experimental with cutter tilt 30°. **a** Surface topography from experimental. **b** Surface topography from simulation with improved Z-MAP algorithm. **c** Surface topography simulation with traditional Z-MAP algorithm. **d** Comparison of section profiles in interval feed direction. **e** Comparison of section profiles in feed direction

surface by cutter tooth, respectively, and the difference of height coordinates (in Z_w-axis) in points Q_ε^* and c^* Δz. In the traditional Z-MAP algorithm, the height coordinate of point c^* is used to express the height coordinate of point Q_ε^*, which causes the error between traditional Z-MAP simulation and experiment bigger than the one between improved Z-MAP simulation and experiment.

Figure 16e shows a section profile in the feed direction. The surface profile fluctuation is relatively larger from experiment due to the sliding and plastic flow of metal cutting layer occurs in the feed direction. The section profile and the R_a basically agreed with simulated by both traditional and improved Z-MAP algorithm; the *RMSE* of section profile simulated by improved Z-MAP algorithm, however, is closer to the

Table 2 The R_a and *RMSE* in interval feed direction and feed direction

Method		Experiment	Simulation		Error	
			Traditional Z-MAP	Improved Z-MAP	Traditional Z-MAP	Improved Z-MAP
Feed direction	R_a (μm)	0.31	0.25	0.28	19%	9.7%
	RMSE (μm)		0.022	0.019		
Interval feed direction	R_a (μm)	1.62	1.57	1.59	3%	1.9%
	RMSE (μm)		0.26	0.24		

measured. In addition, and the 2D profile from improved Z-MAP algorithm is smoother than traditional Z-MAP algorithm, because the improved Z-MAP algorithm uses numerical algorithm to ensure higher precision when calculating the height of the grid point; however, the traditional Z-MAP algorithm introduces the height of a closer discrete point on the cutter tooth to substitute the height of part grid point. The processing costing time of the improved and traditional Z-MAP algorithms are 117.6 and 190.4 s, respectively. Therefore, the improve Z-MAP algorithm constructs an accurate surface profile in 62% of the time required for the traditional Z-MAP algorithm in the vertical milling.

The validation experiments of inclination milling consist of two cases: titling cutter and leading cutter. In inclination milling with the tilting cutter 30°, step over f_p, feed per tooth f_f, cutting depth a_p, spindle speed N, cutter lead angle α, and cutter tooth initial phase angle difference ΔA_i are set 0.5 mm, 0.2 mm, 0.5 mm, 3000 r/min, 0°, and 0°, respectively. Figure 17 shows the surface topographies from simulation and experiment, and the simulation results in Fig. 17b, c are consistent with Fig. 17a, which is from experiments. The comparison of R_a and *RMSE* in interval feed direction and feed direction are in Table 2.

The section profiles from simulation and measured are consistent in interval feed direction, showing differences in the left sides of two summits of surface waviness from Fig. 17d. The reason is that the rotating radius of cutter corresponding to the left side of milled surface peak is smaller when cutter tilt is

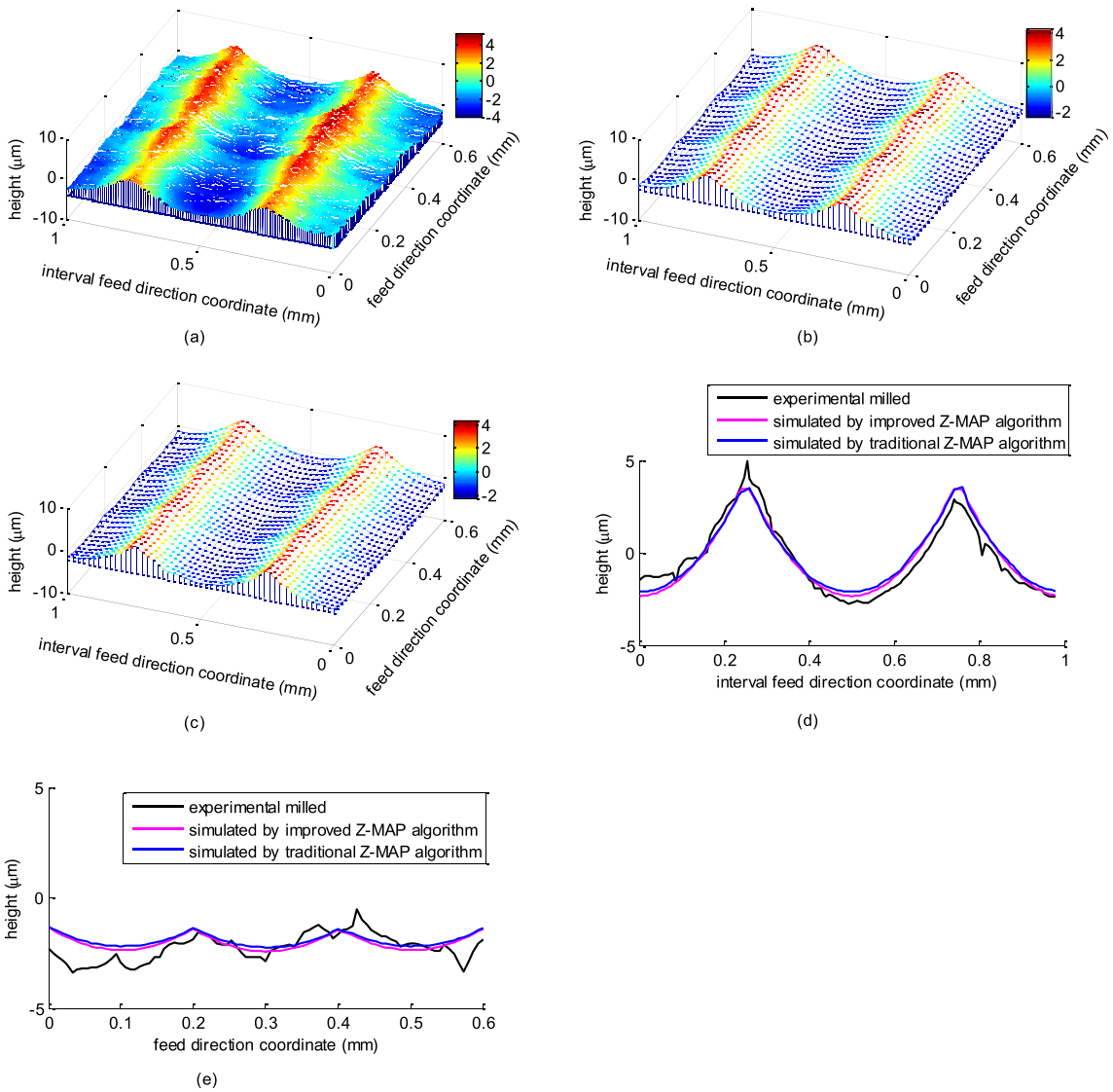

Fig. 18 Comparison between simulated and experimental surface topographies with cutter lead angle 30°. **a** Surface topography from experimental. **b** Surface topography simulated by improved Z-MAP algorithm. **c** Surface topography simulated by traditional Z-MAP algorithm. **d** Comparison of section profiles in interval feed direction. **e** Comparison of section profiles in feed direction

Table 3 The R_a and *RMSE* in interval feed direction and feed direction

Method		Experiment	Simulation		Error	
			Traditional Z-MAP	Improved Z-MAP	Traditional Z-MAP	Improved Z-MAP
Feed direction	R_a (μm)	0.42	0.25	0.35	41%	17%
	RMSE (μm)		0.048	0.045		
Interval feed direction	R_a (μm)	1.62	1.57	1.59	3%	1.9%
	RMSE (μm)		0.26	0.24		

in positive, the cutting velocity is lower accordingly, and then the plastic deformation is large. The R_a from simulation by improved algorithm is closer to the experimental.

Figure 17e shows the section profile trends of simulated and experimental in feed direction that is similar; however, the surface from experimental has many burrs and fluctuations. The reasons are as follows: firstly, sliding and plastic flow of metal in cutting layer happens in feed direction. Secondly, the real shape of ball-end mill cutter tooth, which is like the tooth of saw imprinting on the part surface. Additionally, tearing of cutting chip also causes the appearance of burrs on the milled surface. Similar to the characteristics of section profile in the interval direction, R_a simulated by improved algorithm is closer to the measured, and its *RMSE* is smaller too. The processing time for the improved and traditional Z-MAP algorithms is 106.3 and 175.1 s, respectively. Therefore, the improved Z-MAP algorithm constructs an accurate surface profile in 61% of the time required of traditional Z-MAP algorithm in the inclination milling with title cutter.

The validation experiment of inclination milling by leading cutter with 30° is performed. Step over f_p, feed per tooth f_f, cutting depth a_p, spindle speed N, and cutter tooth initial phase angle difference ΔA_i are set 0.5 mm, 0.2 mm/r, 0.5 mm, 3000 r/min and 0°, respectively. Figure 18 shows the surface topographies from the simulation and experimental. The simulation results in Fig. 18b, c are consistent with Fig. 18a, which is from experiments. The comparison of R_a and *RMSE* in interval feed and feed directions for the inclination milling with lead cutter is in Table 3.

Figure 18d shows the section profiles from simulation and experimental are consistent in interval feed direction, and the R_a and *RMSE* of the section profile simulated by improved algorithm are smaller. Figure 18e shows the section profile variation trends by simulation and experimental are similar in feed direction; however, the experimental has many fluctuations. Besides the reason that the sliding and plastic flow of metal cutting layer mainly occurs in feed direction, the push milling means the friction between the surface machined and the back blade of cutting tooth is increasing when cutter lead angle is positive, and results in the part of material cold welding (like welding in cutting status) on the cutting tooth and form built-up edge, which continuously scratches the milling surface. The built-up edge takes off from the cutter edge when it is increasing to big enough. The dimension of built-up edge is varying in the milling so that there are many random fluctuations left on the surface.

The R_a and *RMSE* of profile simulated by improved algorithm are closer to the experimental one. The processing time by improved and traditional Z-MAP algorithms is 109.7 and 180.4 s. Therefore, the improve Z-MAP algorithm constructs an accurate surface profile in 65% of the time required of traditional Z-MAP algorithm in the inclination milling with leading cutter.

6 Conclusions

According to the fact that ball-end milling cutter machining is extensively used in complicated circumstances, this study focuses on the simulation of machining surface topography of ball-end milling cutter machining, puts forward the improved Z-MAP algorithm for surface topography simulation, discusses the influence rules of various parameters on the surface topography and roughness, and conducts the experiments to compare the performance between improved and traditional Z-MAP algorithm.

(1) The proposed improved Z-MAP algorithm for simulating ball-end milling surface topography, combining the servo rectangular encirclement, angle summation method, and Newton iteration method, based on the ball-end mill cutter tooth movement equation which established on the basis of the transformation principle of homogeneous coordinate matrix in the milling process.
(2) The process parameters', such as feed per tooth, step over, cutter lead angle, cutter tilt angle, and the initial phase angle difference of cutter feed, influence on ball-end milling surface topography is simulated and analyzed by the improved Z-MAP algorithm, and the rules of the influence are obtained which is useful for practical production.

(3) The milling experiments validate the reliability of the proposed algorithm, and the surface topographies from experiment and the traditional and improved Z-MAP algorithm are compared. The results show in both vertical and inclination (with tilting and leading cutter) milling, the simulated surface topography by improved Z-MAP algorithm, the improve Z-MAP algorithm constructs an accurate surface profile in 62%, 61%, and 65% of the time required for the traditional Z-MAP algorithm in the vertical milling, inclination milling with titling cutter and leading cutter.

Funding information The authors wish to thank the financial support for this work from the National Natural Science Foundation of China (51575442), the Shaanxi Natural Science Foundation of China (2016JZ011), the Shaanxi Province Education Department (2014SZS10-Z01), and the Intelligent Systems Center at the Missouri University of Science and Technology.

References

1. Wang HX, Zong WJ, Sun T, Liu Q (2010) Modification of three dimensional topography of the machined KDP crystal surface using wavelet analysis method. Appl Surf Sci 256(16):5061–5068
2. Ait-Sadi H, Hemmouche L, Hattali L, Britah M, Iost A, Mesrati N (2015) Effect of nanosilica additive particles on both friction and wear performance of mild steel/CuSn/SnBi multimaterial system. Tribol Int 90:372–385
3. Imani BM, Elbestawi MA (2001) Geometric simulation of ball-end milling operations. J Manuf Sci Eng 123(2):177–184
4. Sadeghi MH, Haghighat H, Elbestawi MA (2003) A solid modeler based ball-end milling process simulation. Int J Adv Manuf Technol 22(11–12):775–785
5. Liu N, Loftus M, Whitten A (2005) Surface finish visualisation in high speed, ball nose milling applications. Int J Mach Tools Manuf 45(10):1152–1161
6. Liang XG, Yao ZQ (2013) Dynamic-based simulation for machined surface topography in 5-axis ball-end milling. J Mech Eng 06(6): 171–178 **(in china)**
7. Xu AP, Qu YX, Li WM, Zhang DW, Tian H (2001) Generalized simulation model for milled surface topography-application to peripheral milling. Chin J Mech Eng 14(02):121–126
8. Hu W, Guan J, Li B, Cao Y, Yang J (2015) Influence of tool assembly error on machined surface in peripheral milling process. Procedia CIRP 27:137–142
9. Omar OEEK, El-Wardany T, Ng E, Elbestawi MA (2007) An improved cutting force and surface topography prediction model in end milling. Int J Mach Tools Manuf 47(7–8):1263–1275
10. Lavernhe S, Quinsat Y, Lartigue C (2010) Model for the prediction of 3D surface topography in 5-axis milling. Int J Adv Manuf Technol 51(9–12):915–924
11. Zhang C, Zhang H, Li Y, Zhou L (2014) Modeling and on-line simulation of surface topography considering tool wear in multi-axis milling process. Int J Adv Manuf Technol 77(1–4):735–749
12. Franco P, Estrems M, Faura F (2008) A study of back cutting surface finish from tool errors and machine tool deviations during face milling. Int J Mach Tools Manuf 48(1):112–123
13. Yan B, Zhang DW (2001) Modeling and simulation of ball end milling surface topology. J Comput Aided Des Graph 13(2):135–140 **(in china)**
14. Zhao XM, Hu DJ, Zhao GW (2003) Simulation of part surface texture in 5-axis control machining. J Shanghai Jiaotong Univ 37(5):690–694 **(in china)**
15. Zeroudi N, Fontaine M (2012) Prediction of machined surface geometry based on analytical modelling of ball-end milling. Procedia CIRP 1(2012):108–113
16. Liu X, Soshi M, Sahasrabudhe A, Yamazaki K, Mori M (2006) A geometrical simulation system of ball end finish milling process and its application for the prediction of surface micro features. J Manuf Sci Eng 128(1):74–85
17. Han SG, Zhao J, Zhang XF (2009) Surface topography and roughness simulations for 5-Axis ball-end milling. Adv Mater Res 2009(69-70):471–475
18. Zhao HW, Zhang S, Zhao B, Zhang Q (2014) Simulation and prediction of surface topography machined by ball-nose end mill. Comput Integr Manuf Syst 04:880–889 **(in china)**
19. Zhao HW, Zhang S, Wang GQ (2013) Effect of machining inclination angle of ball-nose end mill on surface topography. Comput Integr Manuf Syst 19(10):2438–2844 **(in china)**
20. Bouzakis KD, Aichouh P, Efstathiou K (2003) Determination of the chip geometry, cutting force and roughness in free form surfaces finishing milling, with ball end tools. Int J Mach Tools Manuf 43(5):499–514
21. Antoniadis A, Savakis C, Bilalis N, Balouktsis A (2003) Prediction of surface topomorphy and roughness in ball-end milling. Int J Adv Manuf Technol 21(12):965–971
22. Xu J, Zhang H, Sun Y (2017) Swept surface-based approach to simulating surface topography in ball-end CNC milling. Int J Adv Manuf Technol 5:1–12
23. Peng F, Wu J, Fang Z, Yuan S, Yan R, Bai Q (2013) Modeling and controlling of surface micro-topography feature in micro-ball-end milling. Int J Adv Manuf Technol 67(9–12):2657–2670
24. Jung TS, Yang MY, Lee KJ (2004) A new approach to analysing machined surfaces by ball-end milling, part II. Int J Adv Manuf Technol 25(9–10):841–849